Available online at www.sciencedirect.com
SCIENCE DIRECT®
Journal of Magnetic Resonance 160 (2003) 20–25
JMR Journal of Magnetic Resonance
www.elsevier.com/locate/jmr

Feasibility of probing boundary morphology of structured materials by 2D NMR *q*-space imaging

Chih-Liang Chin,[a] Felix W. Wehrli,[a,*] Scott N. Hwang,[a] Dwight L. Jaggard,[b] David B. Hackney,[c] and Suzanne W. Wehrli[d]

[a] *University of Pennsylvania Medical Center, Laboratory for Structural NMR Imaging, Philadelphia, PA 19104, USA*
[b] *Complex Media Laboratory, Department of Electrical and Systems Engineering, University of Pennsylvania, PA 19104, USA*
[c] *Department of Radiology, 3400 Spruce Street, Philadelphia, PA 19104, USA*
[d] *NMR Core Facility, Department of Radiology, The Children's Hospital of Philadelphia, Philadelphia, PA 19104, USA*

Received 4 April 2002; revised 5 August 2002

Abstract

It is well known that one-dimensional (1D) *q*-space imaging allows retrieval of structural information at cellular resolution. Here we demonstrate by simulation that boundary morphology of structured materials can be derived from 2D *q*-space mapping. Based on a finite-difference model for restricted diffusion, 2D *q*-space maps obtained from water diffusion inside apertures at various levels of asperity were simulated. The results indicate that the observed ring patterns (diffraction minima) reveal the boundary profiles of the apertures but become blurred in the case of significant variation in aperture size. For uniform size distribution of apertures, a quantitative measure of surface roughness can be established by means of spatial autocorrelation analysis. The results suggest that 2D *q*-space imaging may allow probing of the boundary morphology of structured materials and possibly biological cells.

Keywords: NMR; NMR microscopy; *q*-Space; Diffusion; Boundary roughness

1. Introduction

The characterization of heterogeneous systems typically involves retrieval of local morphology which, in turn, determines functional behavior. For example, it has been shown that droplet geometry in oil–water emulsions is linked to the bulk rheology. Similarly, the surface properties of the confining pores in porous media affect fluid transport. In biological systems cell morphology is largely determined by the cells' function and interplay with the local environment. Bulk cell deformation and surface asperity play an important role in cell–cell interaction and cell–substrate adhesion [1]. Recent work has shown that cell shape could serve as a surrogate for classifying the status of disease [2–4]. The knowledge of the shape and size of these structures, which are difficult to visualize directly, is therefore of significant interest.

Previous attempts to quantitatively characterize cell shapes and boundary roughness relied on either electron microscopy [1,5] or scattering measurements [6,7], and a subsequent analysis of the resulting images required the use of geometric models. These approaches are destructive, and often demand extensive specimen preparation and complex image processing procedures. Recently, NMR microscopy has demonstrated its potential for cellular imaging (see, for example [8, Chapter 4]). However, so far, directly resolving cellular structures by NMR microscopy (*k*-space imaging) has been hampered by limited signal–noise ratio (SNR) and the ultimately achievable resolution may be limited by diffusion [9]. These difficulties can under certain circumstances be overcome by NMR *q*-space imaging [10–12], which has been used extensively to retrieve structural information from heterogeneous materials. Specifically, it has been shown that in the presence of confined self-repeating

* Corresponding author. Fax: 1-215-349-5925.
E-mail address: wehrli@oasis.rad.upenn.edu (F.W. Wehrli).

1090-7807/02/$ - see front matter © 2002 Elsevier Science (USA). All rights reserved.
PII: S1090-7807(02)00008-3

structures, the echo attenuation exhibits a diffraction-like pattern resulting from structural refocusing as water molecules encounter barriers while diffusing. The merit of this technique is that, theoretically, a resolution at 0.1–10 μm is achievable, thus providing a vehicle for studying structures not resolvable by conventional k-space NMR imaging. Pulsed-gradient spin echo (PGSE) or pulsed-gradient stimulated echo experiments have been applied to study porous materials and emulsions [8] and, as well as red blood cells [13,14]. More recently, the technique has been exploited to obtain water displacement profiles in the central nervous system of small animals [15,16]. Most prior work aimed at either measuring structure size or regional water displacement profiles was based on one-dimensional (1D) q-space imaging. Such experiments, however, are limited in that they cannot fully characterize structures of lower symmetry.

Recently, it has been shown that by cascading multiple displacement-encoding time intervals (along arbitrary q-vector directions) sequentially it is possible to evaluate the eccentricity of a pore matrix [17]. Likewise, it has been shown that the dispersion of fluid transport can be examined on the basis of time-correlated displacement profiles [18]. The objective of the present work was to assess the feasibility of characterizing cell boundary roughness by examining the diffraction pattern obtained from 2D q-space echo attenuation maps. Toward this goal, PGSE diffusion simulations have been performed for diffusion of water confined inside circular, sinusoidally serrated and fractally serrated aperture arrays. In this context, a numerical method has been developed to quantitatively evaluate boundary roughness from an autocorrelation analysis of the 2D q-space maps.

2. Methods

2.1. Generation of aperture array images with various boundary roughness and size distribution

To simulate biological cells with different levels of boundary roughness, model images of circular, sinusoidally serrated and fractally serrated aperture arrays were generated. For the sinusoidally serrated aperture, the aperture radius, R, possesses a sinusoidal dependence on azimuthal angle, θ,

$$R(\theta) = a + \eta\cos(n\theta), \tag{1}$$

where a is the mean radius, η is the perturbational amplitude ($\eta \ll a$), and n is an integer that determines the period of this sinusoidal variation. It is noted that $\eta = 0$ generates circular apertures. In addition, circular apertures with fractally serrated boundaries were created since fractal analysis has been shown to be useful for assessing cell morphology [2–5]. The concepts of fractals introduced by Mandelbrot [19] embodies the idea of self-similarity and underlying order, which suggests a non-integer fractal dimension, d, that better describes the signature of complex structures. Here we exploit this concept to generate apertures whose boundary roughness can be described by a known fractal dimension. Based on the work by Jaggard et al. [20,21], the band-limited Weierstrass function was used to define the radius of a fractally serrated aperture as

$$R(\theta) = a + \frac{\left\{2\sigma^2\left[1 - b^{(2d-4)}\right]\right\}^{1/2}}{\left[b^{(2d-4)N_1} - b^{(2d-4)(N_2+1)}\right]^{1/2}} \times \sum_{n=N_1}^{N_2} b^{(d-2)n}\cos(b^n\theta + \xi_n). \tag{2}$$

There exist $(N_2 - N_1 + 1)$ spatial frequency components in Eq. (2), and their phase relations are determined by a random variable ξ_n of variance σ^2. The constant b must be chosen as an integer greater than unity, since $R(\theta)$ must be a periodic function with period 2π in order to be continuous. To explore the effect of various degrees of boundary roughness, aperture array images with $d = 1.5$ and $d = 1.99$ were created.

Since the characteristic size of biological cells or porous materials is often heterogeneous, the image of circular apertures with Gaussian size distribution ($\sigma/\mu = 10\%$) was also generated. A specific objective was to investigate the effect of size inhomogeneity on the boundary roughness characterization.

2.2. Relationship between echo attenuation and spin density autocorrelation function

It has been shown that the echo attenuation $E(\mathbf{q}, \Delta)$ and the averaged propagator $\bar{P}(\mathbf{R}, \Delta)$ are Fourier transform pairs ([8, Chapter 7])

$$E(\mathbf{q}, \Delta) = \int \bar{P}(\mathbf{R}, \Delta)\exp[\mathrm{i}\mathbf{q}\cdot\mathbf{R}]\,\mathrm{d}\mathbf{R}, \tag{3}$$

where $\mathbf{q} = \gamma\mathbf{G}\delta$, $\bar{P}(\mathbf{R}, \Delta)$ is the averaged propagator, $\mathbf{R}$ is the displacement vector, $\mathbf{G}$ is the amplitude of the diffusion sensitizing gradient and δ is its duration, and γ is the gyromagnetic ratio. In the case of long diffusion time, i.e., $\Delta \gg a^2/D$, where a is the characteristic length of the structure of interest (here the aperture) and D is the molecular self-diffusion coefficient, the averaged propagator has been shown to approach the autocorrelation function of spin density

$$\bar{P}(\mathbf{R}, \infty) = \int \rho(\mathbf{r})\rho(\mathbf{r} + \mathbf{R})\,\mathrm{d}\mathbf{r}, \tag{4}$$

where $\rho(\mathbf{r})$ is the spin density function. From the Wiener–Kintchine theorem it further follows that the echo attenuation can be expressed as:

$$E(\mathbf{q}, \infty) = |S(\mathbf{q})|^2, \tag{5}$$

where $|S(\mathbf{q})|^2$ is the Fourier power spectrum of spin density from which the shape of the apertures can be

derived without the need to obtain the displacement image [10]. For example, for a unit circular aperture, *circ*(**r**), the 2D Fourier power spectrum would be a $(jinc)^2$ function [22]

$$\mathrm{circ}(\mathbf{r}) \equiv \begin{cases} 1, & \leqslant 1, \\ 0, & \mathbf{r} > 1, \end{cases} \tag{6}$$

$$|B\{\mathrm{circ}(\mathbf{r})\}|^2 = \left|2\pi \int_0^1 \mathbf{r} J_0(2\pi \mathbf{r}\mathbf{v})\, \mathrm{d}\mathbf{r}\right|^2 = \left|\frac{J_1(2\pi \mathbf{v})}{\mathbf{v}}\right|^2, \tag{7}$$

where **r** is the radius, $B\{\}$ represents the Fourier–Bessel transform, **v** is the radius in Fourier conjugate space, and J_0 and J_1 are the Bessel functions of the first kind with order 0 and 1, respectively.

Since in the limit where $\Delta \to \infty$ $|S(\mathbf{q})|^2 \to |S(\mathbf{k})|^2$ one may wonder why the same information could not be obtained by *k*-space imaging. However, the latter yields far less SNR, which results from phase spread across the entire field-of-view due to spatial encoding. In contrast, *q*-space imaging encodes spin displacement, no absolute spatial information required, thus the phase spread is limited to local motion (diffusion). Therefore, in *q*-space imaging, the trade-off for the loss of phase information is higher SNR.

2.3. Simulation of 2D q-space echo attenuation maps

q-Space imaging simulations were performed by using an algorithm developed by Hwang et al. [23]. The method was based on a finite difference model approximation of the diffusion equation, in which the NMR signal was calculated for the PGSE sequence at echo time. A pulse sequence diagram is shown in Fig. 1. This approach has previously been validated for restricted diffusion bounded by parallel planes and diffusion within a sphere, where the numerical results agreed well with existing analytical solutions.

The model circular, sinusoidally serrated, and fractally serrated aperture arrays, described above, served as input for the simulations. Each image consisted of a 200×200 matrix, with a pixel size of $0.865\,\mu m^2$, covering a 5×5 array of non-permeable circularly shaped elements of 29.76 μm mean diameter. The interior of the elements was assumed to be occupied by water while the interstices were assumed to be empty. The diffusion sensitizing gradients were oriented along two orthogonal axes on the image plane (*x* and *y* direction). Imaging parameters were TR/TE = 1000/65 ms, $\delta/\Delta = 3/60$ ms, and for the diffusion coefficient of the water a value of $2.5\,\mu m^2$/ms was chosen. The 2D *q*-space was covered by stepping diffusion gradients in 16 increments from 0 to 75 G/cm, with a 5 G/cm linear increment for each *x* and *y* direction, resulting in 256 *q*-space samples covering the first quadrant of 2D *q*-space, which suffices for structures of fourfold symmetry as is the case for circular and sinusoidally serrated apertures. However, for the fractally serrated apertures having only twofold symmetry, two adjacent quadrants of *q*-space must be sampled. The magnetization was calculated and updated for each time step (0.04 ms) up to the echo time, and echo magnitude of the NMR signal, *S*, was obtained by summing the transverse magnetization from each pixel. Finally, the 2D *q*-space echo attenuation map was created by plotting the logarithm of echo amplitude ratio, $\ln(S/S_0)$, where S_0 is the echo amplitude in the absence of diffusion sensitizing gradient versus *q*. The *q*-space quadrants not sampled were filled by making use of the known symmetry relationships; yielding a 31×31 data matrix. All diffusion simulations were carried on an Apple MacIntosh PowerPC G4 computer (800 MHz) with 512 MB memory using a computer program written in C (CodeWarrior, Metrowerks, Austin, TX, USA), while simulations of model aperture array images and the calculations of 2D *q*-space maps were performed in interactive data language (IDL, Research Systems, Boulder, CO, USA).

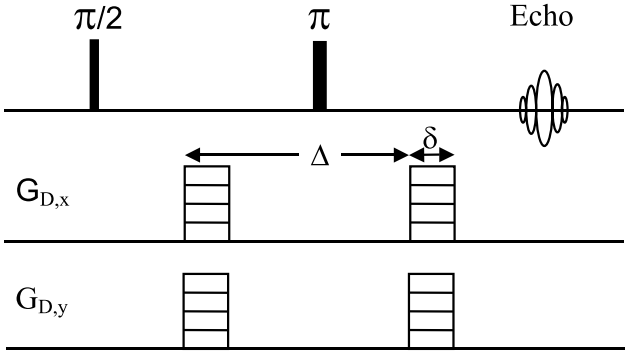

Fig. 1. PGSE pulse sequence used for 2D *q*-space imaging.

2.4. Quantification of boundary roughness by autocorrelation analysis of 2D q-space maps

In optical experiments, diffraction patterns from a circular aperture consist of rings (corresponding to diffraction minima and maxima), which are self-repeating radially, possessing no angular dependence. However, as the boundary of the aperture becomes rough, the diffraction pattern begins to deviate from this simple behavior. We therefore postulate that boundary roughness of simulated apertures may be quantifiable by spatial autocorrelation analysis of 2D *q*-space maps. To this end, the calculated *q*-space data were first transformed from rectangular (q_x, q_y), to polar coordinates, (q_r, q_θ), by linear interpolation. This operation resulted in 32 linearly incremented values, increasing radially from 0 to $q_{r\_\max}$ (corresponding to $G_r = 75$ G/cm), with 64 angular increments, spaced equally between 0 and π radians. Subsequently, the autocorrelation function, AFC(*l*), along the radial direction, was calculated for

each specified angle, θ, followed by averaging over all selected angular orientations:

$$\mathrm{ACF}(l) = \frac{1}{N_\theta}\sum_{\theta}\left\{\sum_{k=0}^{N_r-1-l}(r_k-\bar{r})(r_{k+l}-\bar{r}) \Big/ \sum_{k=0}^{N_r-1}(r_k-\bar{r})^2\right\}, \quad (8)$$

where, $\bar{r}$ is the mean of N_r echo-attenuation values at angle θ, l is the lag ($l = 0, 1, \ldots, N_r - 2$), $N_r = 32$, and $N_\theta = 64$.

3. Results and discussion

3.1. Model aperture array images and calculated 2D q-space maps

Figs. 2A–D show model images of arrays with varying boundary roughness (mean aperture diameter = 29.76 μm, pixel width = 0.93 μm), along with calculated 2D q-space maps (Figs. 2F–I), displayed after interpolation from 31×31 to 124×124. The rings (diffraction minima) of the q-space maps at low q-values reflect the gross shape of the aperture, while the fine structure is embedded in high q-values. This observation

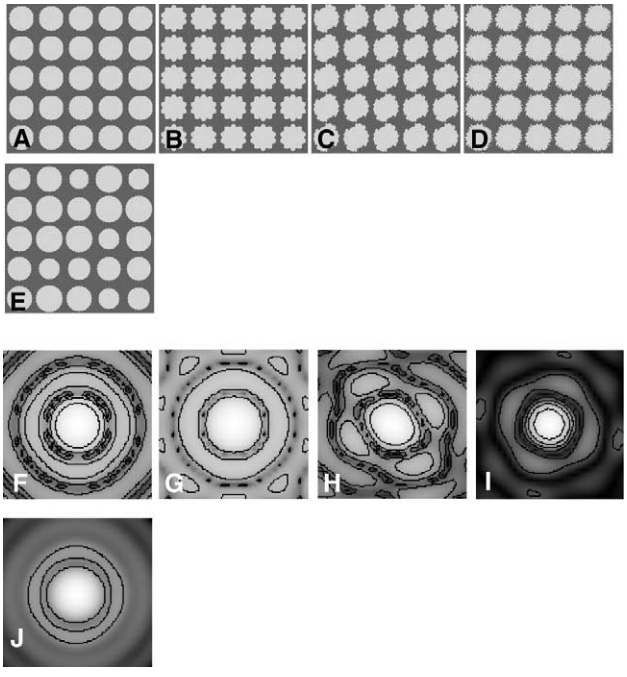

Fig. 2. Array of model apertures (A)–(E) and corresponding simulated 2D q-space maps (F)–(J). Circular (Fig. A, $\eta = 0$); sinusoidally serrated (Fig. B, $\eta/n = 1.48/10$); fractally serrated (Fig. C, $d = 1.5$) and (Fig. D, $d = 1.99$), where $\sigma/b/N_2/N_1 = 1.6/2/20/1$ and ξ satisfies a uniform distribution within [0,1]. The 2D q-space maps (Figs. F–J) have been linearly interpolated from 31×31 to 124×124 for display, with q_x and q_y values ranging from -958 to $958\,\mathrm{cm}^{-1}$.

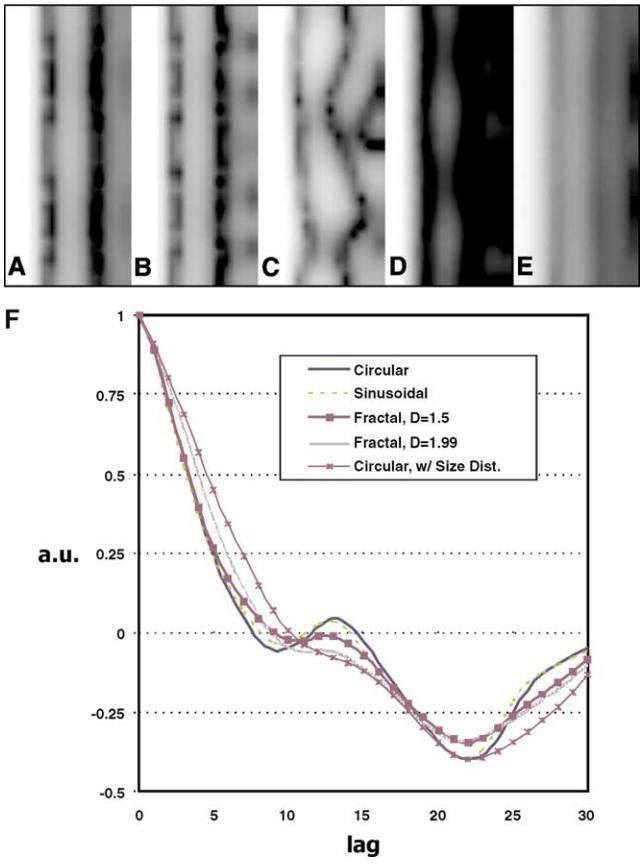

Fig. 3. (A)–(E) Transformed 2D q-space maps in which horizontal and vertical axes represent q_r [0, $q_{r\_\max}(= 958\,\mathrm{cm}^{-1})$] and q_θ [0, π]. Maps have been linearly interpolated from 32×64 to 128×256. (F) Results of autocorrelation analysis for various boundaries (A)–(E), plotted with each curve normalized to its maximum value and a unit lag corresponding to $\Delta q_r = 31\,\mathrm{cm}^{-1}$.

is analogous to k-space where high k-values delineate high spatial frequency information. The superimposed contour plots reveal aperture shape and allow distinction between circular and sinusoidally serrated apertures (Figs. 2F and G). For the data of the fractally serrated aperture array (Figs. 2H–I), the diffraction rings lose their circular appearance and eventually vanish at high q-values as a result of loss of structural coherence, although the averaged aperture shape is still evident at the center of q-space. Further, the superimposed contour plots indicate increased angular dependence with increasing boundary asperity. However, as the roughness increases further, the angular dependence is lost, and the pattern reflects only gross object shape. This finding agrees with the optical experiments by Kim et al. [21], who showed that the preferential orientation of diffraction rings disappears as the aperture's boundary roughness increases.

Fig. 2E shows the image of circular array in which the aperture diameter satisfies a Gaussian distribution ($\mu = 30.20$ μm; $\sigma = 2.98$ μm). The corresponding interpolated 2D q-space map is displayed in Fig. 2J. The ring

Table 1
Calculated slopes and roughness indices from autocorrelation plots

Aperture	Circular	Sinusoidal	Fractal, $d = 1.5$	Fractal, $d = 1.99$
Slope, S [$\times 10^{-2}$]	2.414	1.699	0.711	0.283
S/S_c[a]	1	0.704	0.295	0.117
RI[b]	1	1.152	1.530	1.932

[a] S_c is the slope calculated from circular aperture.
[b] $RI = 1 - \log(S/S_c)$.

pattern is still present; however, significant blurring of the rings caused by the variation in aperture size is apparent. The q-space map results from the superposition of the calculated diffraction patterns of each individual aperture.

3.2. Quantitative analysis of boundary roughness

Fig. 3 shows the transformed diffraction patterns displayed in polar coordinates. This display mode provides a different perspective for qualitatively assessing boundary roughness. The observed dark bands represent the diffraction minima as a function of polar angle and radius. For the circular apertures (Fig. 3A), the dark bands clearly possess no angular dependence, in contrast to Fig. 3B, showing five isolated patches in the high q-value region. These diffraction minima correspond to the five angular positions at greatest radial distance of the sinusoidal aperture in the range of $[0, \pi]$, as a result of the reciprocal relationship between q-value and displacement. The emerging dark band is expected to vary sinusoidally in intensity as q-values increase. Further, the wavy dark bands shown in Fig. 3C represent the boundary profile of the fractally serrated aperture. However, no fine structure can be seen in Fig. 3D due to the very high boundary roughness ($d = 1.99$). Similar to Fig. 3A, the dark bands observed for the circular aperture array with Gaussian size distribution still preserve independence of polar angle. However, the heterogeneity in structure size causes significant signal attenuation in high q-value regions.

The calculated autocorrelation functions, derived from the q-space data of Figs. 3A–E, are shown in Fig. 3F. The curve with the narrowest width of the first maximum (following the parent peak) is associated with the circular aperture. However, as boundary roughness increases, the peak broadens. In addition, the autocorrelation plot derived from the data in Fig. 3E indicates that, when the structure size varies, no second maximum is present and correlation merely manifests as a shoulder.

As a possible means to quantitatively characterize boundary roughness, the slope S between the first minimum and second maximum of the autocorrelation curve was calculated, yielding a roughness index, RI, defined as $RI = 1 - \log(S/S_c)$, where S_c represent the slope calculated for the circular aperture. Table 1 lists the calculated slopes and roughness indices. Interestingly, the roughness index parallels fractal dimension. This observation suggests that the calculated autocorrelation function may provide a measure of self-similarity of the boundary profile at different q-values (displacement scale). Nevertheless, the current method is sensitive to the uniformity of structure size and will fail for significant heterogeneity in structure size.

Recent experimental work on biological cells by q-space imaging did not involve shape analysis. Torres et al. [14] applied 1D q-space spectroscopy to erythrocytes indicates differences in the diffusion–diffraction plots and a dependence on apparent cell diameter for various pathological conditions. However, no attempts were made to derive cell shape from the q-space plots. The 2D q-space maps could thus potentially be applied to monitor the morphological variations of cells due to disease or the changes in the environmental conditions. For example, axonal swelling observed in spinal cord injury will cause the rearrangement of intra-axonal and extra-cellular space. However, significant hurdles will have to be overcome to apply the q-space method to biological structures. Among these are membrane permeability, size, and orientation distribution of structures, and interference of structural refocusing from intra- and extra-cellular restricted diffusion that has been shown to affect the echo attenuation amplitude [14,24]. More importantly, the interplay of these effects needs to be considered carefully when interpreting q-space data. For example, in the study of yeast cell morphology, the orientation and size distribution effects can be separated by a multiple NMR scattering approach [17]. Clearly, to more realistically assess the feasibility of the present approach in biological cells, our current model needs to be refined by including cell membrane permeability and the contributions from both intra- and extra-cellular diffusion.

4. Conclusions

Simulations reported in this work suggest that 2D q-space imaging allows quantitative assessment of boundary roughness in arrays of apertures of uniform size distribution. Such information can be retrieved in

situations where SNR limitations render *k*-space imaging impractical. The targeted application to biological cells is complicated by finite permeability of the boundaries, structural heterogeneity and the presence of diffusing water in all compartments.

Acknowledgments

NIH research Grant RO1 NS41380.

References

[1] J.L. Mege, C. Capo, A.M. Benoliel, C. Foa, R. Galindo, P. Bongrand, Quantification of cell surface roughness; a method for studying cell mechanical and adhesive properties, J. Theor. Biol. 119 (1986) 147–160.
[2] G.A. Losa, G. Baumann, T.F. Nonnenmacher, Fractal dimension of pericellular membranes in human lymphocytes and lymphoblastic leukemia cells, Pathol. Res. Pract. 188 (1992) 680–686.
[3] T.F. Nonnenmacher, G. Baumann, A. Barth, G.A. Losa, Digital image analysis of self-similar cell profiles, Int. J. Biomed. Comput. 37 (1994) 131–138.
[4] B. Nielsen, F. Albregtsen, H.E. Danielsen, The use of fractal features from the periphery of cell nuclei as a classification tool, Anal. Cell Pathol. 19 (1999) 21–37.
[5] K.M. Keough, P. Hyam, D.A. Pink, B. Quinn, Cell surfaces and fractal dimensions, J. Microsc. 163 (1991) 95–99.
[6] D.E. Burger, J.H. Jett, P.F. Mullaney, Extraction of morphological features from biological models and cells by Fourier analysis of static light scatter measurements, Cytometry 2 (1982) 327–336.
[7] M. Bradaczek, H. Guski, H. Bradaczek, G.G. Avtandilov, Determination of the structure of tissue samples using X-ray small angle scattering, Pathol. Res. Pract. 196 (2000) 827–830.
[8] P.T. Callaghan, Principles of Nuclear Magnetic Resonance Microscopy, Oxford University Press, Oxford, 1993.
[9] Z.H. Cho, C.B. Ahn, S.C. Juh, H.K. Lee, R.E. Jacobs, S. Lee, J.H. Yi, J.M. Jo, Nuclear magnetic resonance microscopy with 4-microns resolution: theoretical study and experimental results, Med. Phys. 15 (1988) 815–824.
[10] D.G. Cory, A.N. Garroway, Measurement of translational displacement probabilities by NMR: an indicator of compartmentation, Magn. Reson. Med. 14 (1990) 435–444.
[11] P.T. Callaghan, A. Coy, D. MacGowan, K.J. Packer, F.O. Zelaya, Diffraction-like effects in NMR diffusion studies of fluids in porous solids, Nature 351 (1991) 467–469.
[12] G.A. Barrall, L. Frydman, G.C. Chingas, NMR diffraction and spatial statistics of stationary systems, Science 255 (1992) 714–717.
[13] P.W. Kuchel, A. Coy, P. Stilbs, NMR "diffusion–diffraction" of water revealing alignment of erythrocytes in a magnetic field and their dimensions and membrane transport characteristics, Magn. Reson. Med. 37 (1997) 637–643.
[14] A.M. Torres, R.J. Michniewicz, B.E. Chapman, G.A. Young, P.W. Kuchel, Characterization of erythrocyte shapes and sizes by NMR diffusion–diffraction of water: correlations with electron micrographs, Magn. Reson. Imaging 16 (1998) 423–434.
[15] Y. Assaf, A. Mayk, Y. Cohen, Displacement imaging of spinal cord using *q*-space diffusion-weighted MRI, Magn. Reson. Med. 44 (2000) 713–722.
[16] M.D. King, J. Houseman, D.G. Gadian, A. Connelly, Localized *q*-space imaging of the mouse brain, Magn. Reson. Med. 38 (1997) 930–937.
[17] Y. Cheng, D.G. Cory, Multiple scattering by NMR, J. Am. Chem. Soc. 121 (1999) 7935–7936.
[18] S. Stapf, R.A. Damion, K.J. Packer, Time correlations in fluid transport obtained by sequential rephasing gradient pulses, J. Magn. Reson. 137 (1999) 316–323.
[19] B.B. Mandelbrot, The Fractal Geometry of Nature, W.H. Freeman, New York, 1983.
[20] D.L. Jaggard, Y. Kim, Diffraction by band-limited fractal screens, J. Opt. Soc. Am. A 4 (1987) 1055–1062.
[21] Y. Kim, H. Grebel, D.L. Jaggard, Diffraction by fractally serrated apertures, J. Opt. Soc. Am. A 8 (1991) 20–26.
[22] J.W. Goodman, Introduction to Fourier Optics, McGraw-Hill, New York, 1996.
[23] S.N. Hwang, F.W. Wehrli, D.B. Hackney, A finite difference model for simulating restricted diffusion in the spinal cord, in: Proc. Int. Soc. Magn. Res. Medicine, Eighth Scientific Meeting, Denver, USA, 2000, ISMRM 762.
[24] C.L. Chin, F.W. Wehrli, S.N. Hwang, D.B. Hackney, S. L. Wehrli, Feasibility of measuring axon size in the rat spinal cord by *q*-space imaging: effect of membrane permeability and cell size distribution, in: Proc. Int. Soc. Magn. Res. Medicine, Ninth Scientific Meeting, Glasgow, Scotland, UK, 2001, ISMRM 1516.